

Northumbria Research Link

Citation: Liu, Bang-Yan, Chen, Li-Jen, Seemann, Ralf and Brinkmann, Martin (2019) Directional liquid wicking in regular arrays of triangular posts. *Langmuir*, 35 (50). pp. 16476-16486. ISSN 0743-7463

Published by: American Chemical Society

URL: <https://doi.org/10.1021/acs.langmuir.9b03032>
<<https://doi.org/10.1021/acs.langmuir.9b03032>>

This version was downloaded from Northumbria Research Link:
<http://nrl.northumbria.ac.uk/id/eprint/41587/>

Northumbria University has developed Northumbria Research Link (NRL) to enable users to access the University's research output. Copyright © and moral rights for items on NRL are retained by the individual author(s) and/or other copyright owners. Single copies of full items can be reproduced, displayed or performed, and given to third parties in any format or medium for personal research or study, educational, or not-for-profit purposes without prior permission or charge, provided the authors, title and full bibliographic details are given, as well as a hyperlink and/or URL to the original metadata page. The content must not be changed in any way. Full items must not be sold commercially in any format or medium without formal permission of the copyright holder. The full policy is available online: <http://nrl.northumbria.ac.uk/policies.html>

This document may differ from the final, published version of the research and has been made available online in accordance with publisher policies. To read and/or cite from the published version of the research, please visit the publisher's website (a subscription may be required.)



**Northumbria
University**
NEWCASTLE



UniversityLibrary

Directional liquid wicking in regular arrays of triangular posts

Ban-Yang Liu ^{a,b}, Ralf Seemann ^b, Li-Jen Chen ^a, and Martin Brinkmann ^{b*}

(a) Department of Chemical Engineering, National Taiwan University, 10617 Taipei, Taiwan

(b) Experimental Physics, Saarland University, 66123 Saarbrücken, Germany

Abstract: Wicking of wetting liquids into micro-patterns of posts with homogeneous triangular cross-section is studied in experiments and by numerical energy minimizations. To test for directional wicking we fabricated regular arrays of posts with various combinations of line fractions and aspect ratios using standard photolithography processes. In agreement with numerical energy minimizations of the liquid film morphology, we find spontaneous wicking in the experiments only for line fractions and aspect ratios where the homogeneous liquid film represents the state of lowest interfacial free energy and where no local energy minimum could be detected in our numerical energy minimizations. The numerical results further demonstrate that the stability of a certain morphology of the terminal meniscus controls the direction of wicking relative to the orientation of the triangular posts. The observed selectivity of spontaneous wicking in respect to the meniscus orientation can be exploited to build a micro-fluidic rectifier for partially wetting liquids.

Keywords: Wetting of micro-patterned surfaces, wicking, directional wetting

* martin.brinkmann@physik.uni-saarland.de

Introduction

The water repellent Lotus leaves are prominent examples of how topographic micro-structures can drastically change the adhesion and motion of liquids on a surface ¹. Micro-structures creating a bias for liquids to move into certain directions have been found on butterfly wings ², the needles of the cactus *Opuntia microdasys* ³, and the skin of the lizard *Phrynosoma cornutum* ⁴. Both, the cactus and the lizard are adapted to life in a highly arid habitat, and their survival relies on an effective collection and uptake of rain and dew water. A directional liquid transport to the snout of the lizard has been demonstrated in experiments using a model skin with replicated surface features ⁴.

Directional wetting phenomena on artificial microstructures have been described for arrays of slender micro-posts bend to one side ⁵ and topographic micro-patterns created by photolithography in combination with suitable modulations of the surface energy ⁶. These surfaces could be tuned to show uni-, bi-, and tri-directional spreading of partially wetting liquid. Liquids deposited on chemically homogeneous solid surfaces decorated with micro-patterns of parallel grooves may display anisotropic droplet shapes or even spread solely parallel to the grooves ⁷⁻¹⁰.

Anisotropic wetting and wicking of liquids on topographically patterned surfaces is not amenable to simple thermodynamic arguments. Wenzel's angle of a rough and chemically homogeneous solid surface, for instance, refers to the apparent contact angle of a droplet that attains the global minimum of interfacial energy for a given volume. Apart from the corrugations of the three phase contact line, which scale with the length of the heterogeneities, the global shape of an asymptotically large droplet is a hemispherical cap. Hence, by construction, the Wenzel angle does not depend on the local orientation of the interface with respect to an anisotropic surface pattern.

Equilibrium shapes of sessile droplets wetting micro-patterned surfaces are controlled by the magnitude of interfacial pinning forces which depend on the orientation of the three phase contact line relative to the micro-pattern. A dense spectrum of local energy minima and energy barriers trap, or 'pin', the interface more or less effectively for certain orientations.

Similar to the anisotropic equilibrium shapes of macroscopic sessile drops, spontaneous wicking of a liquid film into a regular array of topographic surface features is potentially governed by the

orientation of the terminal meniscus of the film relative to the micro-pattern. The anisotropy of pinning forces found on regular surface patterns manifests in the strong faceting of wicking liquid films¹¹. Micro-patterns of periodically repeated posts with a broken reflection symmetry, such as triangular posts, not only display directional wicking in experiments¹² and in fluid dynamics simulations¹³ but can also be easily created by photolithographic techniques.

In the present work, we consider the condition for liquid wicking in rectangular arrays of posts with an equilateral triangular cross-section. The centers of the triangular posts are arranged in a rectangular unit cell, while the bases of the triangles are aligned with one of the lattice directions. Figure 1(a) shows the profile of a micro-pattern employed in our experiments measured by confocal microscopy. An example of a heptane film wicking such a micro-pattern is provided in Fig. 1(b). Heptane was chosen as test liquid because the material contact angle of heptane with the surface of our samples slightly larger than 45° and, thus, falls into a range where a competition of different modes of interfacial advance are expected¹⁴.

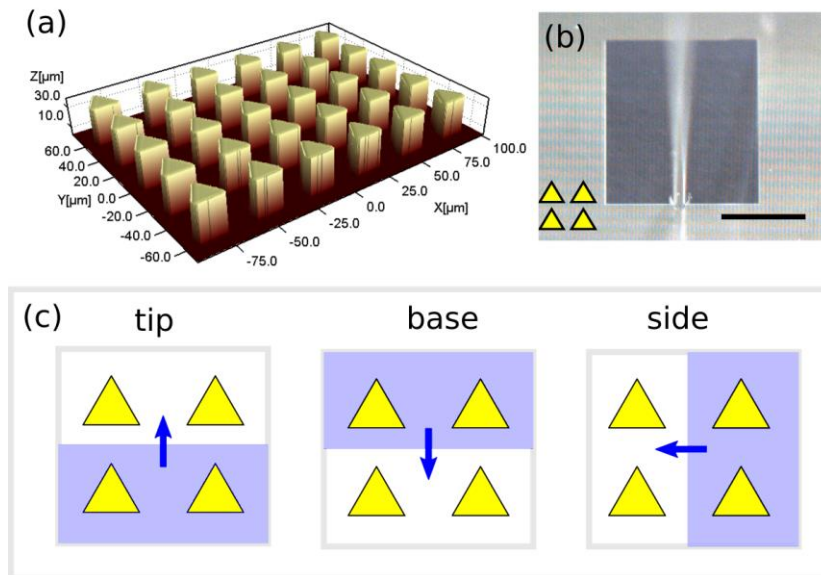


Figure 1. (a): White-light interferometry image of experimentally investigated topographic micro-pattern of triangular posts. (b): Optical reflection microscopy image showing the example of a heptane film wicking in tip and side direction ($LF \approx 0.46$, $AR \approx 2.6$). While the advancement of the film in tip orientation is faster than in side orientation, the motion into base direction is completely blocked. The liquid is provided via a hollow needle that is also visible on the image. The length bar denotes 2 mm (c): Moving terminal meniscus oriented in tip, base, and side orientation.

It is already apparent from the shape of the wicked area shown in Fig.1(c) that the terminal meniscus of a film may not move into all three possible directions of the pattern with the same non-zero velocity. In sparse arrays of posts with low aspect ratio, like in the example Fig. 1(b), the advancement of the terminal meniscus may be even fully blocked. On some of our samples we find that only the direction of the triangle base is blocked while liquid spontaneously advances into tip and side directions.

To gain further insight into the physical mechanisms that govern directional wicking we studied the morphology and stability of the terminal meniscus of a liquid film at different orientations relative to the triangular posts array in numerical energy minimizations. In combination with a thermodynamic consideration, the numerically determined regions where no stable terminal meniscus can be found provide a criterion for spontaneous wicking which fully explains our experimental findings.

Methods

Experimental: The geometry of the topographic micro-patterns illustrated in Fig. 2 is uniquely characterized by the vertical line fraction $VLF = a/r$, being the ratio of height a of the equilateral triangle and period r of rows, the lateral line fraction $LLF = w/c$, defined as the ratio of post width and period c of columns, and the aspect ratio $AR = h/w$ of post height h and post width. Unless otherwise stated, we consider post arrays with equal line fractions into lateral and vertical direction $VLF = LLF$ and simply refer to the line fraction of the posts as LF . Choosing equal line fractions in both lattice directions also implies that the ratio of vertical to horizontal period $r/c = \sqrt{3}/2$ is identical to the height to base ratio of the triangular cross-section, $a/w = \sqrt{3}/2$, cf. also Fig. 2(b). Using this definition of the post geometry, and provided that $VLF = LLF$, the gaps between posts of both neighboring rows and columns close when the line fraction tends to unity.

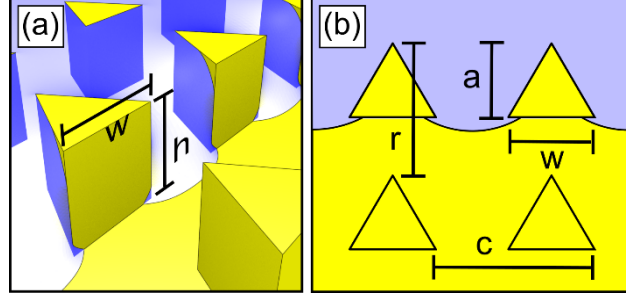


Figure 2. (a): Three dimensional rendering of a terminal film meniscus indicating the aspect ratio $AR = h/w$. The substrate is shown in yellow, the wetting liquid in transparent blue. (b): Both, the lateral line fraction $LLF = w/c$ and the vertical line fraction $VLF = a/r$ of the equilateral triangular posts are chosen to be $\sqrt{3}/2$.

Regular arrays of posts with equilateral triangular cross-section and various aspect ratios AR and line fractions LF are fabricated by standard UV photolithography: Plane glass surfaces are spin-coated with SU-8 photoresist (Kayaku Advanced Materials, Inc., MA, USA), cured thermally, exposed to UV light through a chromium mask, post-exposure baked, and then developed to resolve the triangular micro-posts in the resin. We followed the process parameters (such as, spin speed, UV exposure dose, bake temperature...) proposed in the SU-8 datasheets (<https://kayakuam.com/products/su-8-photoresists/>) with minor modification adapting our system to prepare the micro-patterned SU-8 substrates. A chemically resistant and homogeneous surface with desired wetting properties for wicking experiments is achieved by subsequently coating the SU-8 surface pattern with a Teflon AF layer (Teflon AF 1061S, DuPont). Prior to the experiments, we characterized the final surface topography of such fabricated micro-patterned substrates with an optical microscope (Olympus, BXFM) and by confocal microscope (KEYENCE, VK-X210), cf. also the example in Fig. 1(a). The side length of the triangular posts in all samples is fixed to $w = (18.5 \pm 0.5) \mu\text{m}$. The distances r and c are varied to obtain line fractions of the post arrays between $LF = 0.180 \pm 0.002$ and 0.857 ± 0.024 . For each line fraction, we fabricated samples with various structure heights corresponding to aspect ratios between $AR = 0.680 \pm 0.028$ and $AR = 2.77 \pm 0.09$. As it is expected that the AF coating of the SU-8 structures is not quite as perfect as on the smooth SU-8 reference surface, it can be assumed that both the advancing and the receding contact angles in the surface pattern are slightly lower.

Heptane is employed as a testing liquid for the wicking experiments; its advancing and receding contact angle on a Teflon AF coated flat SU-8 reference surface are $\theta_a = (51.6 \pm 1.0)^\circ$ and $\theta_r = (42.7 \pm 1.2)^\circ$, respectively. Contact angles of heptane are determined with the embedded needle method¹⁵ using an in-house developed enhanced video-microscopy system and digital image analysis tool¹⁶. Heptane is used as a testing liquid as its desired wetting properties allow to experimentally map out all possible (directional) wicking scenarios by varying the post geometries within our experimental fabrication limits.

To perform a wicking experiment, we first place a hollow needle with a flat tip at a distance of about 0.1 mm above the micro-patterned surface. The small gap between the needle tip and the substrate ensures a gentle first contact of the extruded liquid with the substrate which minimizes the influence of the liquid impact on the following dynamics. Heptane is injected at a rate of 5 $\mu\text{L}/\text{min}$. This rate is sufficient to over-compensate the loss of mass due to evaporation at the beginning of a wicking experiment but might be balanced by evaporation at a later time after the area covered by wetting film has increased. During injection, the contour of the liquid interface is simultaneously recorded in top and side view.

Numerical model: Owing to a lack of continuous symmetries of the wetted substrate and the free interface like, e.g., the axial symmetry of barrel droplets on cylindrical fibers¹⁷, the equilibrium shapes of a liquid in contact to a periodic micro-pattern can only be determined with the help of numerical methods. Throughout this work, we compute the morphology and stability of the terminal meniscus of the liquid film in a sharp interface model using finite elements. Stable shapes of the interface are obtained by numerical energy minimizations (NEM) of the interfacial energy. While phase field models bear the advantage of allowing topological changes of the liquid-air interface during wicking or de-wicking, they require a small ratio of intrinsic interface width to the size of the surface topographies. But owing the high resolution of the interface region that is required to correctly reproduce the observed macroscopic wetting phenomena, the diffuse interface models are not suited to quantitatively assess the mechanical stability of the terminal meniscus.

In view of the experiments, we consider the particular situation of a wicking liquid film which is connected to a sessile droplet with a diameter being large compared to typical dimension L of

the micro-pattern. As we are working with surface features of typical dimensions $L < 100 \mu\text{m}$ and with heptane with an interfacial tension $\gamma_{lv} = 20 \text{ mN/m}$ a density $\rho = 684 \text{ kg/m}^3$ at 20°C , the Bond number $Bo = \rho g L^2 / \gamma_{lv}$ is always smaller than $1.5 \cdot 10^{-3}$ in the present experiments where we assume an acceleration of gravity $g = 9,81 \text{ m/s}^2$. The typical length scale L is given by the maximum of the lattice period r, c , base width w , and height of the posts, h . Because the Bond number is far smaller than unity, we can safely neglect contributions of gravity to the total free energy of the liquid.

Direct contributions of van der Waals interactions or further short ranged interactions become relevant only for feature sizes well below a micrometer¹⁸. Thus, over a wide range of length-scales, from micrometers up to a millimeter, the shape of a liquid interface in equilibrium is governed solely by interfacial energies, and we can safely neglect any contribution of hydrostatic pressure or disjoining pressure to the local Laplace pressure.

Since the wicking liquid film is in equilibrium with a large droplet that acts as a liquid reservoir we can set the Laplace pressure in the film to zero also in the following numerical investigations. Under these conditions, any stable equilibrium conformation of the free liquid interface Σ_{lv} is a local minimum of the interfacial free energy:

$$E = \gamma_{lv}A_{lv} + \gamma_{sl}A_{sl} + \gamma_{sv}A_{sv}, \quad (1)$$

where $\gamma_{\alpha\beta}$ and $A_{\alpha\beta}$ are the interfacial free energy per unit area and the area of the interfaces, respectively, between liquid (l), vapor (v), and solid (s). Since the total surface area $A_s = A_{ls} + A_{vs}$ of the non-deformable solid surface is constant, we can drop the constant energy term $\gamma_{sv} A_s$ in Eqn. (1). Expressing the difference $\gamma_{sv} - \gamma_{sl}$, through $\gamma_{lv} \cos \theta_0$ by virtue of the definition of Young's contact angle θ_0 , we can rewrite the interfacial free energy Eqn. (1) in the form:

$$E = \gamma_{lv}(A_{lv} - \cos \theta_0 A_{ls}). \quad (2)$$

Throughout this work we compute the shape of locally stable interfacial configurations with NEM using the freely available software Surface Evolver¹⁹. The fundamental idea behind the approach of the Surface Evolver is that the surface of the solid in contact to the liquid and to the vapor phase, Σ_{ls} and Σ_{sv} , respectively, as well as the three phase contact line between liquid, solid

and vapor, Γ_{lv} , are uniquely determined by the shape and position of the free interface Σ_{lv} . In the numerical model of the wicking film, the shape of the liquid–vapor interface is approximated by a mesh of triangles spanning a set of nodes. In such a representation by finite elements, the interfacial energy is a function of the $3N$ coordinates of the nodes of the mesh, and can be minimized by a variety of optimization algorithms available in the Surface Evolver¹⁹. Nodes of the mesh that represent the shape of the three phase contact lines are subject to local geometrical constraints, as they have to stay in the surface of the substrate. Contributions to the interfacial free energy related to the solid surface in contact to the liquid are computed from line integrals of suitably chosen functions over the closed contact line¹⁹.

Motivated by the experimental result that the terminal meniscus is always fully aligned with the lattice directions, cf., e.g., Fig 1b, we restrict our numerical study to only three relative orientations of the terminal meniscus with respect to the post arrays, as illustrated in Fig. 1(c). The discrete symmetries of the micro-pattern allow us to reduce the costs of the numerical calculations.

We suppose that the wetting liquid forms a film of uniform thickness identical to the height of the posts at some distance behind the terminal meniscus. A film state with a homogeneous thickness that matches the vertical extensions of the post will be state of lowest free energy per area provided the post spacing is sufficiently small and the posts are sufficiently tall.

In the present case, it is not restrictive to assume that the base of the posts all lie in the plane $z = 0$ and to compute only a half period of the liquid interface by exploiting the supposed reflection symmetry of the free interface with respect to the plane at $y = 0$. To account for possible local energy minima for the same control parameters values of that differ in the topology of their liquid–vapor interface, we designed a series of initial interface configurations in the numerical model, each equipped with a plausible interfacial topology. We cannot completely rule out the possibility to find more interfacial topologies leading to physically valid local energy minima in the numerical model, i.e. equilibrium configuration of the free interface that are neither self-intersecting nor penetrating into the solid surface.

To determine the regions of geometric control parameters line fraction LF and aspect ratio AR where certain meniscus morphologies are mechanically stable and compatible with the geometry of the micro-pattern, we follow the corresponding local minimum of the interfacial energy while

the control parameters are changed in small steps. After each change, a sufficient number of gradient descends and re-meshing steps are applied to ensure that the interfacial configuration stays close to the local energy minimum. During their tracking, the local energy minima may approach a saddle point and vanish at certain points in the space of control parameters. These points bound the regions in the space of control parameters where certain mechanically stable configuration of the terminal meniscus are found.

Results

Based on our experimental observations for samples with various line fractions and aspect ratios of the triangular posts, the shape of the heptane-air interface may evolve in three different ways after being brought into contact with the micro-pattern.

In the first case, we observe asymmetric droplets sitting on the array of triangular post, as can be seen in the side view and top view Fig. 3(a) and (b), respectively. The apparent advancing contact angle of the heptane interface in tip orientation for this particular micro-pattern is found to be 48° , smaller than the value of 64° measured in base orientation. No indication of a heptane film penetrating into the micro-pattern around the droplet base is found.

In the second case, a homogenous heptane film forms whose terminal menisci in tip, in base, and in side orientation progress, cf. Fig. 3(c). In this wicking scenario the liquid neck between the needle and the micro-patterned surface has a negative curvature as expected for a negative Laplace pressure at a progressing leading edge of a wicking film. The rectangular film area in top view Fig. 3(d) shows that the dynamics of wicking depends on the relative orientation of the terminal meniscus of the film with respect to the triangular posts. Generally, the velocity of the terminal meniscus is faster in tip orientation as compared to side orientation. The example in Fig. 3(d) shows further that wicking is faster in left side orientation as compared to right side orientation, which could result from slight geometrical variations caused by the manufacturing process.

In the third case, directional wicking of a heptane film is observed in only two of three possible orientations of the terminal meniscus (tip and side), cf. the reflection microscopy image in Fig. 1(b). Whenever directional wicking is observed on a sample, the terminal menisci in tip and side orientation are moving while terminal menisci in base orientation stay permanently arrested.

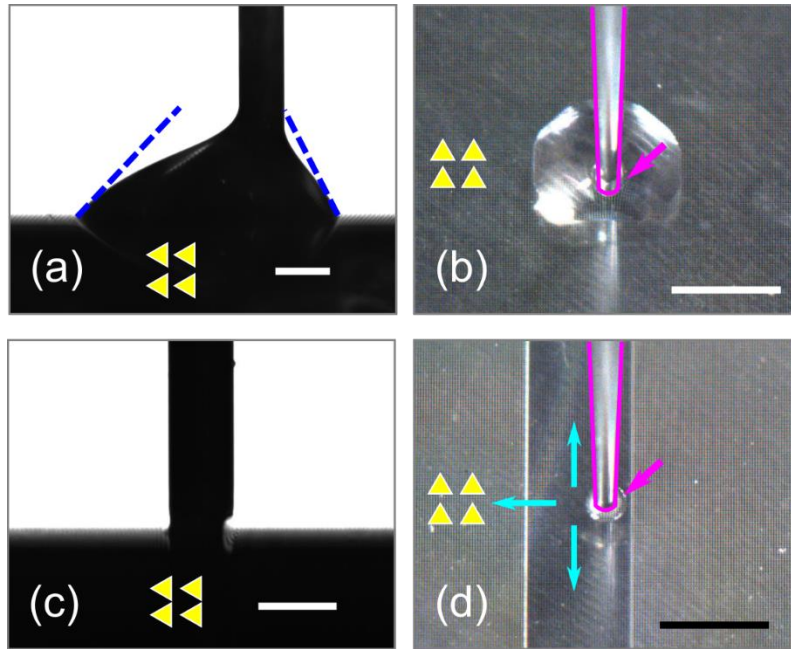


Figure 3. Images of wicking experiments in side view (a,c) and in top view (b,d). Yellow triangles show the alignment of the posts array. Both post arrays in the top row (a,b) and in the bottom row (c, d) have the same line fraction $LF \approx 0.37$, but different aspect ratios $AR \approx 0.7$ for (a,b) and $AR \approx 2.8$ for (c,d). The heptane film in (d) appears as dark grey. Steel needles and their tip positions are highlighted by a magenta outline. Blue arrows in (d) indicate the directions of wicking (tip, base, and left side). Ideally, both side orientations should be equivalent but the reflection symmetry of the micro-pattern may be broken by slight imperfections of the post geometry. Scale bars represent 0.5 mm in (a), (c) and 2 mm in (b) and (d).

To explore the general ability of a liquid to form a wicking film or a sessile droplet, we conducted numerical energy minimizations with the surface evolver for a Young's contact angle of $\theta_0 = 50^\circ$ with the substrate of the micro-pattern that is very close to the advancing contact angle of our testing liquid, heptane. In any of the three cases discussed above, the terminal meniscus of a wicking film as well as the lateral interface of a droplet in our experiments is fully aligned with the lattice direction of the post array. This observation justifies the restriction of our numerical investigations to individual terminal menisci of the liquid film that are oriented in one of the lattice directions as shown in Fig.1(c).

For all three considered orientations of the terminal meniscus with respect to the posts, and for all considered post geometries and wetting conditions, we observe two fundamentally different morphologies of the terminal meniscus in our numerical energy minimizations. The morphologies are distinguished by the position and topology of the three phase contact lines at the terminal

meniscus, cf. also Fig. 4. In the *coalesced meniscus morphology* Fig. 4(a), the three phase contact line in front of the pillars is located entirely on the bottom plane of the substrate, while in the *pinned meniscus morphology* Fig. 4(b), the outermost three phase contact line makes excursions onto the sidewalls of the posts. Contact lines of different topology shown in Fig. 4 are highlighted in green and magenta.

For a given material contact angle, each of the two equilibrium morphologies of the film edge (coalesced or pinned) is restricted to a certain range of line fractions and aspect ratios of the post array. To illustrate the mechanisms limiting this range of accessible control parameters let us imagine that we had the possibility to slowly change the geometry of the micro-pattern and to follow simultaneously the shape of the terminal meniscus in a local energy minimum. Micro-patterns with a tunable line fraction have been realized, for example, in wetting experiments using elastically stretchable sheets ^{20,21}.

The *coalesced meniscus morphology* will be destabilized and decay as soon as the meniscus touches the back of the posts in the next row before the terminal meniscus, see Fig. 4(a) left. First, the furthestmost part of three phase contact line will touch the foot of a post in the row of dry posts ahead of the meniscus. As the liquid interface forms a material contact angle $\theta_0 < 90^\circ$ on the vertical wall of the post in equilibrium, a negative mean curvature is imposed to the interface close to the post such that the resulting gradient of the Laplace pressure will draw more liquid from the film into the region around the post. As a consequence of the local volume increase, the three phase contact line slides up the vertical wall until it becomes pinned to the top edge of the post. Simultaneously to the upward motion, the liquid is also drawn into the edges formed by the vertical sidewalls of the posts and the bottom plane.

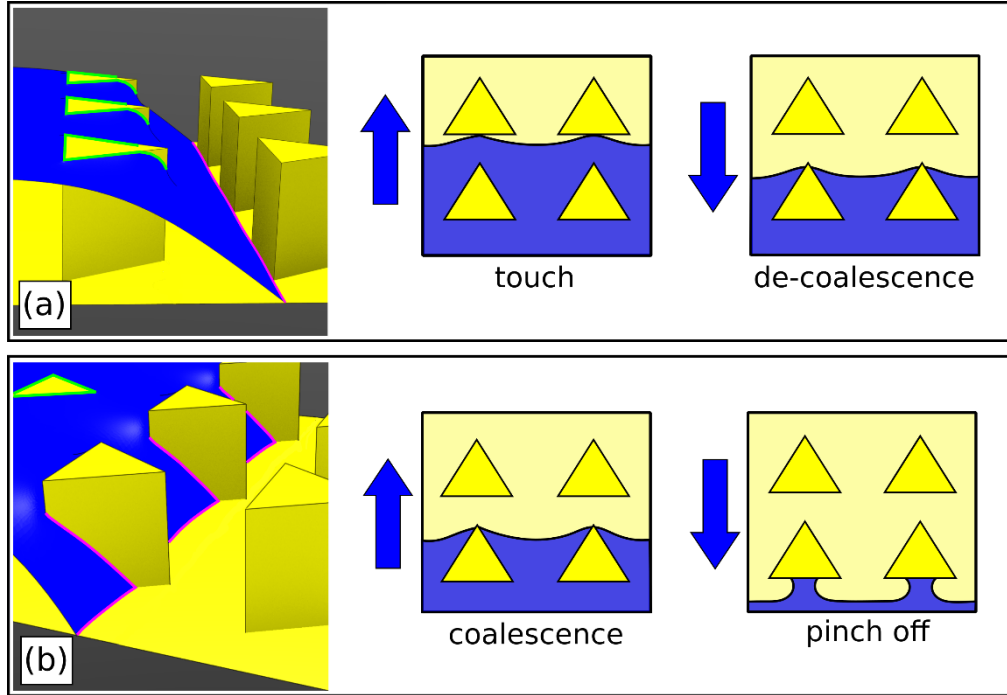


Figure 4. Example for the two equilibrium morphologies of the terminal meniscus obtained in our numerical energy minimizations. Shown are (a) a coalesced terminal meniscus, and (b) a pinned terminal meniscus. The outermost three phase contact line and the contact lines wrapping around the side walls of the posts are highlighted in magenta and in green, respectively. As sketched in the cartoons right of the renderings, each of the two equilibrium morphologies can be destabilized in two different ways, leading to a meniscus advance to the next row of posts or to a meniscus retraction to the previous row of posts, respectively. For the particular topology in (a), the three phase contact line Γ_{lsv} of the ultimate row of posts in contact to the film forms non-connected closed loops (green lines).

The second type of instability a meniscus of the coalesced morphology may undergo is a de-coalescence of the interface and three phase contact line ahead of the post. The de-coalescence instability is observed only for retracting terminal menisci of the coalesced morphology. While the retracting contact line approaches the tip of the posts, the liquid film in front of the tip thins and finally ruptures, leading to a change of the interface topology of the terminal meniscus. During this process, the three phase contact lines that wrap around the posts of the outermost wet row (shown in green in Fig. 4) break up and connect to the continuous three phase contact line segment in the bottom plane of the substrate (cf. the magenta lines in Fig. 4).

Similar to the coalesced meniscus morphology, the range of control parameters where the *pinned meniscus morphology* is mechanically stable is limited by two further interfacial instabilities. The first instability the pinned morphology may undergo is the coalescence of the terminal meniscus of ahead of the posts. This coalescence is observed only if the terminal meniscus of the pinned morphology advances. The coalescence instability is highly sensitive to the contact angle because the terminal meniscus significantly protrudes into the right angled wedges formed by the bottom plane and the side walls only if the material contact angle is sufficiently close to, or below 45° . For a material contact angles lower than 45° , one observes spontaneous spreading along the complete length of the right angled wedges at the base of the posts^{14,22} which implies that the terminal meniscus in equilibrium is always in the coalesced morphology.

The second instability the pinned meniscus morphology may encounter is a pinch-off of the liquid from the back of the posts. This pinch-off instability occurs only during a receding motion of a terminal meniscus in the pinned morphology. A typical feature of the pinch-off instability is the formation of a liquid neck between the back of the post and the film in the next row of posts, resembling the well-known Rayleigh-Plateau instability of a free-standing liquid cylinder.

At this point it is worth mentioning that the specific series of events described for the coalescence instability of the pinned meniscus and the touch instability of the coalesced meniscus should be observed not only during adiabatically slow changes of the control parameters. An alternating sequence of transient non-equilibrium states of the terminal meniscus in the pinned and coalesced morphology similar to the ones following a coalescence and touch instability, respectively, will be found also during spontaneous wicking in the case of fixed control parameters. An analogous statement can be made also for spontaneous de-wicking of the film where the transient non-equilibrium states of the pinned and coalesced morphology are subject to pinch-off and de-coalescence, respectively.

In the following, we will summarize the regions in the plane spanned by line fraction $LF = w/c = a/r$, and aspect ratio $AR = h/w$ of the posts where certain morphologies of the terminal meniscus exist as local minima of the interfacial energy for a given material contact angle θ_0 in terms of stability diagrams. For the sake of clarity, we will present and discuss the numerically determined stability diagrams for terminal menisci in tip, in side, and in base orientation separately

but for the same material contact angle of $\theta_0 = 50^\circ$. Numerical results on the stability of terminal meniscus for Young contact angles in the range of 45° and 52° will be presented later in this section.

Tip orientation: As mentioned above, interfacial configurations belonging to the coalesced morphology and the pinned morphology may undergo two fundamentally different types of instabilities during a continuous change of the control parameters line fraction LF and aspect ratio AR . Stable coalesced morphologies can be found only in the hatched band in Fig. 5a. While increasing the line fraction LF and the aspect ratio AR , a terminal meniscus of coalesced morphology ceases to exist due to a touch instability on the dashed (red) line in Fig. 5 (a). Along this line in the morphology diagram the three-phase contact line of the terminal meniscus touches the pillars in front and the liquid will flow along the edges of the post base formed by the vertical sidewalls and the bottom plane. This process may lead to a coalescence of the liquid film ahead of the posts in tip direction unless the aspect ratio of the posts is very high. When decreasing LF and AR of the post array, the de-coalescence instability of the coalesced meniscus morphology occurs along the solid (black) line in Fig. 5(a).

Stable pinned meniscus morphologies exist in the parameter space defined by the narrow hatched region in the stability diagram of Fig. 5(b). The pinned meniscus morphology will be destabilized towards large line fractions LF and large aspect ratios AR by coalescence when approaching the dashed-dotted (magenta) line in Fig. 5(b). The dotted (blue) stability line in Fig. 5(b) is limiting the range of mechanically stable pinned menisci to small LF and small AR by the pinch-off of the interface from the flat back side of the posts.

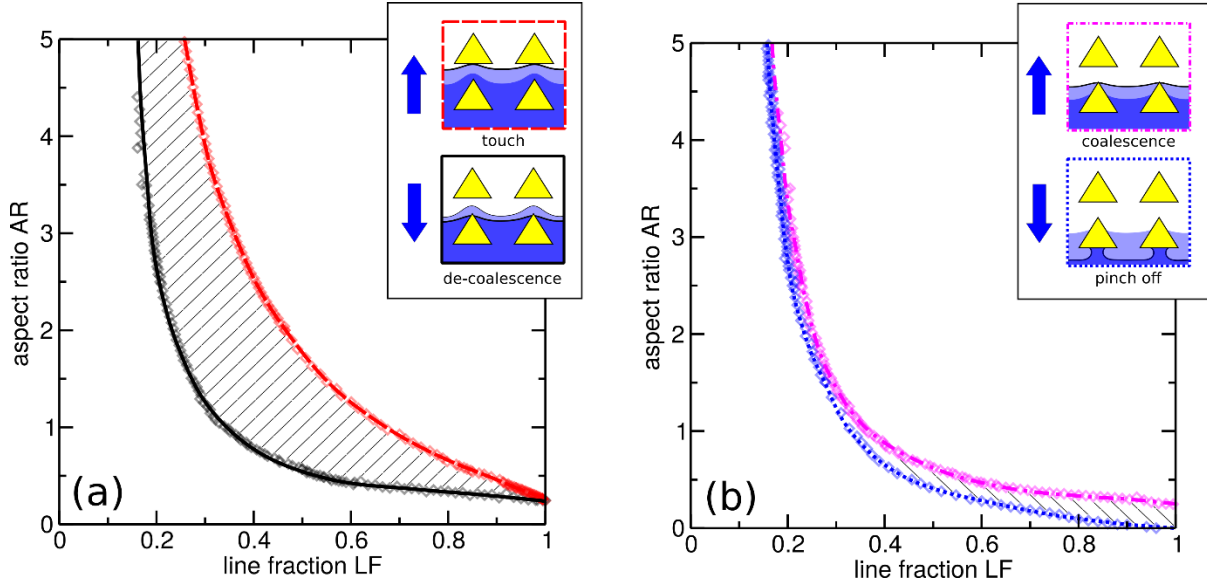


Figure 5. Numerically determined stability diagrams of (a) the coalesced meniscus morphology and (b) the pinned meniscus morphology in tip orientation for a Young's angle of $\theta_0 = 50^\circ$. Hatched areas indicate regions where the respective morphology is mechanically stable. Symbols denote boundaries with respect to the instability mechanism indicated in the inset, lines represent polynomial fits to the numerical data.

Both stability boundaries, i.e. the touch and the de-coalescence line of the coalesced meniscus morphology appear to reach the same finite aspect ratio of $AR \approx 0.25$ in the limit $F \rightarrow 1$. In the opposite limit $LF \rightarrow 0$ the aspect ratio of the touch and the de-coalescence line appear to diverge. The same is found for the pinch-off line and coalescence line of the pinned meniscus morphology. In the limit $LF \rightarrow 1$ also the coalescence line approaches the same finite aspect ratio of $AR \approx 0.25$. The pinch-off line, however, tends to $AR = 0$ as $LF \rightarrow 1$.

Base orientation: The touch and de-coalescence instabilities govern the range of mechanically stable coalesced menisci not only in tip direction but also in the opposing base orientation, cf. the hatched region in Fig 6 (a). Starting again with a stable coalesced meniscus morphology, during a continuous increase of the line fraction LF , the terminal meniscus, and with it the three phase contact line on the lower substrate plane, approach the tip of the post in the row ahead, and the stable coalesced meniscus morphology undergoes a touch instability (red data in Fig. 6 (a)). For a meniscus in base orientation, and for the value of Young's contact angle $\theta_0 = 50^\circ$ considered here, the touch boundary line terminates together with the de-coalescence boundary line (black data in Fig. 6 (a)) at a point $(LF, AR) \approx (0.65, 1.32)$. Hence, the coalesced meniscus morphology

cannot be observed at any aspect ratio of the posts if the line fraction exceeds the value $LF \approx 0.65$. In the limit $LF \rightarrow 0$, however, both the de-coalescence line and touch line grow monotonously. Consequently, the range of stable coalesced menisci in Fig. 6 (a) forms a tongue-shaped region. Note that the transitions along both boundaries are discontinuous and that the end point of the lines is not a bifurcation (critical) point of the energy landscape. If the touch instability were absent, as for a terminal meniscus that wets the outermost row of posts in the array, the de-coalescence line would continue to larger line fractions.

Mechanically stable pinned meniscus morphologies in base direction are found in a much wider range of line fractions LF and aspect ratios AR as compared to pinned menisci with an orientation in tip direction. It is apparent from the stability diagram shown in Fig. 6 (b) that the stability boundary related to coalescence asymptotes to a vertical line while approaching a line fraction of $LF \approx 0.46$ from below, cf. the u-shape of the dash-dotted (magenta) coalescence line in the stability diagram shown in Fig. 6 (b). This particular feature of the coalescence line implies that the pinned meniscus morphology can be observed for arbitrarily large aspect ratio provided the lateral line fraction of the posts exceeds the threshold value of $LF \approx 0.46$. The line limiting the range of mechanically stable pinned menisci to small LF and small AR by pinch-off in Fig. 6 (b) has a similar shape as the stability limit for menisci in tip direction, cf. blue line in Fig. 5 (b). The u-shape of the stability boundary related to the coalescence instability in combination with the stability line for pinch-off creates a re-entrant stability region. Hence, the region of line fractions and aspect ratios where the pinned meniscus morphology in base orientation is mechanically stable is substantially larger than in tip orientation. A re-entrant region of stability of similar shape has been previously found in numerical investigations of meniscus morphologies in regular array of square posts¹⁸.

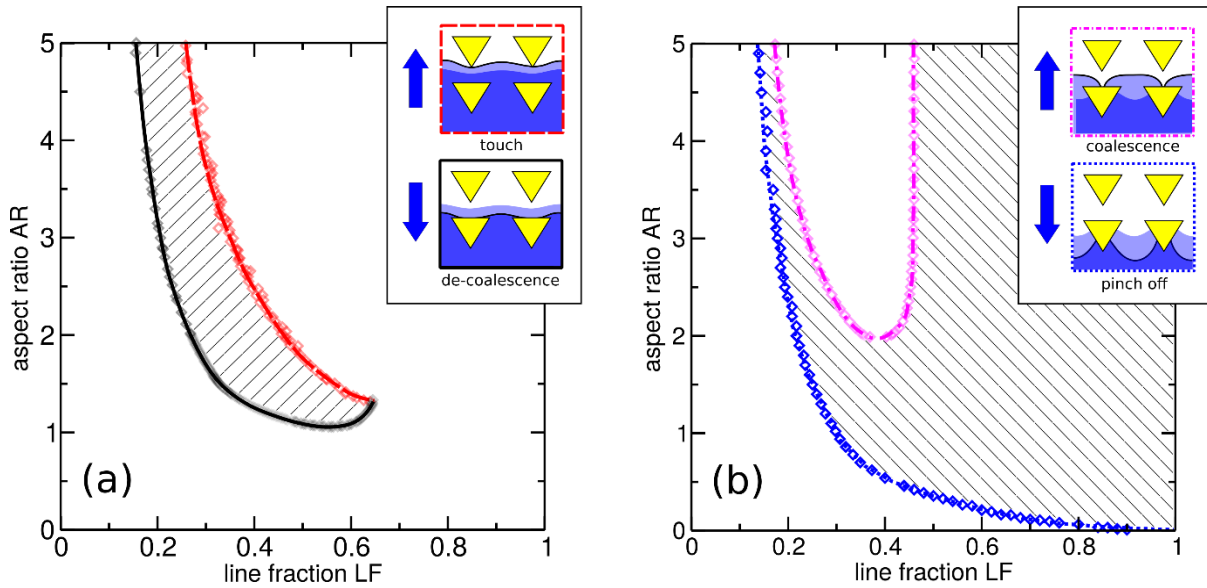


Figure 6. Numerically determined stability diagrams of (a) the coalesced meniscus morphology and (b) the pinned meniscus morphology in base orientation for a Young's angle of $\theta_0 = 50^\circ$. Hatched areas indicate regions where the respective morphology is mechanically stable. Symbols denote boundaries with respect to the instability mechanism indicated in the inset, lines represent polynomial fits to the numerical data.

Side orientation: Coalesced and pinned meniscus morphologies as local energy minima are also found for terminal menisci oriented in side direction. All four types of interfacial instabilities touch, de-coalescence, pinch-off, and coalescence are encountered also in side direction. The stability diagram shown in Fig. 7 (a) reveals that the coalesced meniscus morphology can be found in a band of intermediate line fraction LF and aspect ratio AR . This band is limited by the touch instability to large LF and large AR , and by the de-coalescence instability to small LF and small AR . Qualitatively, the shape of the region of locally stable coalesced menisci resembles the shape of the corresponding region for a meniscus in tip orientation, cf. Figs.5 (a). In the limit of dense post arrays $LF \rightarrow 1$, the touch and de-coalescence line tend to aspect ratios $AR \approx 0.24$ and $AR \approx 0.22$, respectively. The coalescence line and the pinch-off line in Fig. 7 (b) approach aspect ratios $AR \approx 0.4$ and $AR \approx 0$, respectively, for $LF \rightarrow 1$. Overall, the stability diagram of the pinned meniscus morphology in side direction Fig. 7 (b) resembles the corresponding diagram in tip direction Fig. 5 (b).

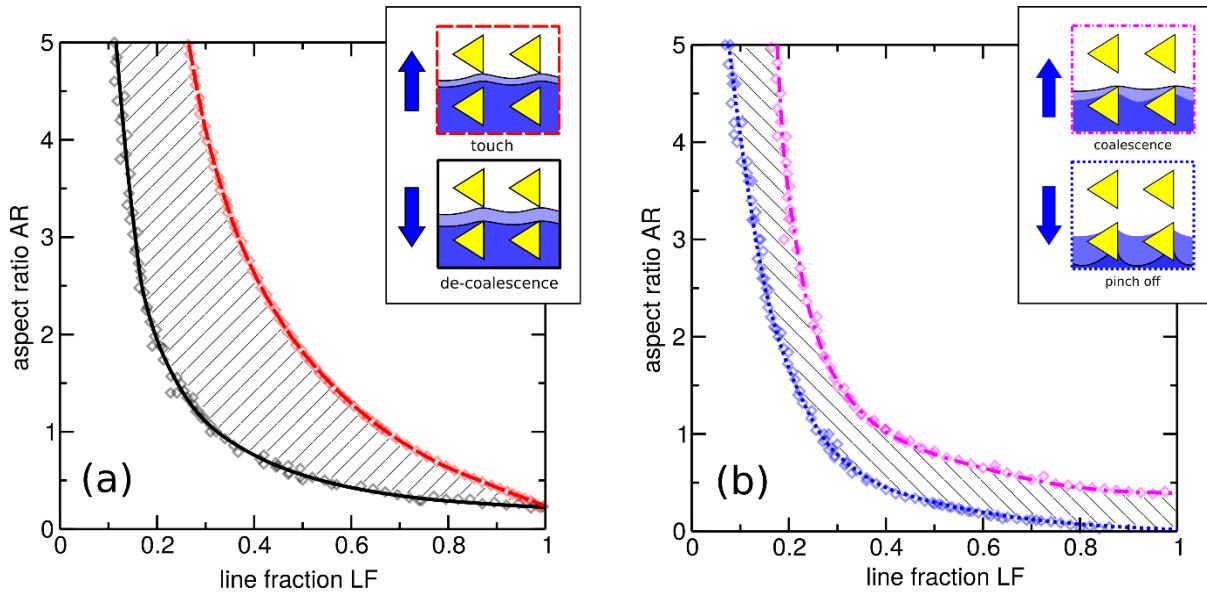


Figure 7. Numerically determined stability diagrams of (a) the coalesced meniscus morphology and (b) the pinned meniscus morphology in side orientation for a Young’s angle of $\theta_0 = 50^\circ$. Hatched areas indicate regions where the respective morphology is mechanically stable. Symbols denote boundaries with respect to the instability mechanism indicated in the inset, lines represent polynomial fits to the numerical data.

Conditions for directional wicking: To identify the regions of line fractions LF and aspect ratios AF that give rise to directional wicking, we first need to superimpose the regions of mechanically stable pinned and coalesced meniscus morphologies. Spontaneous wicking or de-wicking can only be reliably observed in regions of the (LF, AF) - plane where the moving front of the liquid film cannot be trapped in one of the two stable meniscus morphologies.

Figure 8 (a-c) shows the combined stability diagrams for menisci in tip, base, and side orientation, respectively. For all three meniscus orientations, the stability lines of the pinned meniscus with respect to a pinch-off instability (dotted blue) and of the coalesced meniscus with respect to the touch instability (dashed red) are close, i.e., the latter two instabilities are rather insensitive to the relative orientation of the meniscus. Only the coalescence line of the pinned meniscus (dash dotted magenta) and the de-coalescence line (solid black) of the coalesced morphology in base orientation Fig. 8 (b) differ significantly from the respective stability boundaries of menisci in tip and side orientation Fig. 8 (a,c).

In addition to regions where at least one of two meniscus morphologies is stable, there are also regions of the line fraction and aspect ratio in the stability diagrams Fig. 8 (a-c) where no mechanically stable meniscus shape exist. In general there are two non-connected regions of that kind for every relative orientation, one for small line fractions LF and small aspect ratios AF (blue area) and another one for large LF and large AF (red area). The respective regions where stable meniscus shapes are absent display a similar shape for tip, base, and side orientation. Only the region for large LF and large AF in base orientation differs qualitatively from the corresponding regions for menisci in tip and side orientation.

To decide which of the unstable regions are related to wicking of de-wicking, we indicate in Fig. 8(a-c) as green lines the points in the (LF, AR) - plane where the dry state and the “complete” film whose thickness matches the vertical extensions of the posts have equal interfacial free energies. Above and to the right of the green line, e.g., for large LF and AR , the complete liquid film gains energy by progressing further into the dry post array. Left below the green line of equal interfacial energy in the stability diagrams of Fig. 8, i.e., for small values of LF and AR , the complete film gains free energy during retraction, provided there is no liquid left behind. With this information at hand, we hypothesize that de-wicking occurs for parameter ranges left and below the (bi-) stable regions and correspondingly that wicking occurs right and above the (bi-) stable regions, respectively, in the small tongue shaped region extending from top in case of a meniscus in base orientation.

The idea that the dry and the complete film state are the only possible global energy minima is restricted to a certain range of contact angles. For a Young’s contact angle $\theta_0 < 45^\circ$ in the limit of sparse and flat posts the dry state represents only a metastable state for a vanishing Laplace pressure. In this case, states with isolated or coalesced liquid rings around the base of the posts have a lower interfacial free energy. We cannot exclude that such an “incomplete” or “perforated” film state could still represent a local or even the global energy minimum for contact angle $\theta_0 > 45^\circ$ in a certain geometry of the posts.

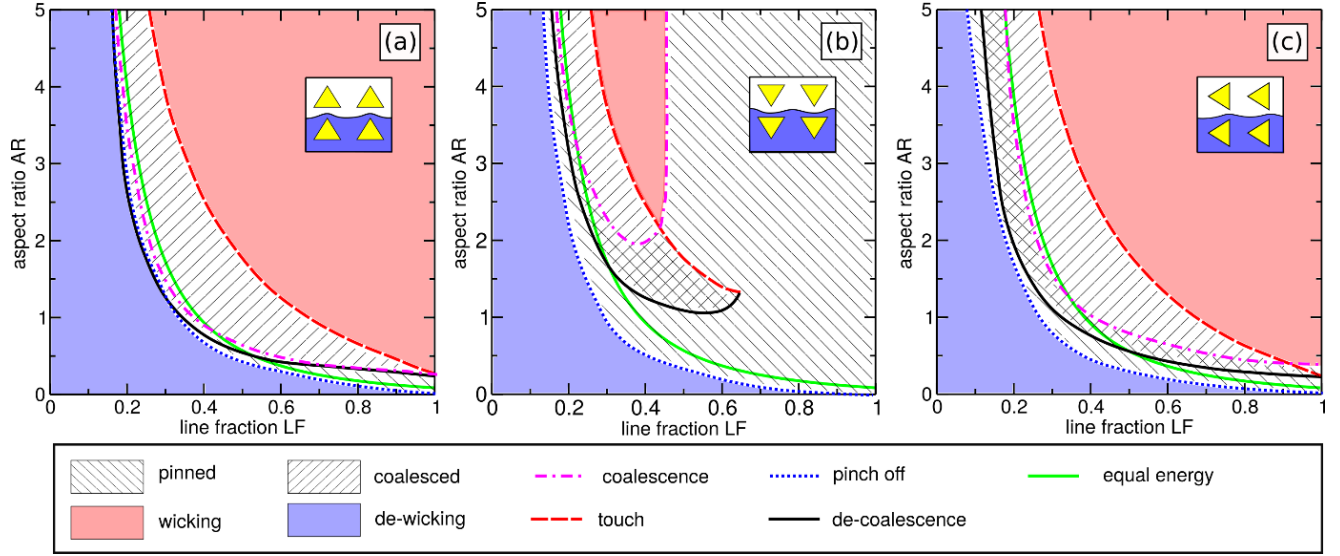


Figure 8. Combinations of the stability regions and limiting instabilities of the terminal meniscus in terms of the line fraction LF and aspect ratio AR of the triangular posts as discussion in Figs. 4, 5, and, 6 for (a) tip, (b) base, and (c) side orientation, Regions where the coalesced and pinned meniscus morphology represent local minima of the interfacial energy are shown as hatched areas. The green lines indicates the points where the interfacial energy of the film and the dry state are equal. Spontaneous wicking is observed in the red area while spontaneous de-wicking is found in the blue area.

The appearance and stability of certain meniscus morphologies, and, following our central hypothesis, the regions of spontaneous wicking and de-wicking, are controlled not only by the line fraction LF and aspect ratio AR of the posts but also by the value of Young's contact angle θ_0 itself. Figure 9 summarizes the influence of the exact value of Young's contact angle on the hypothesized regions of wicking, i.e., where the film state has a lower free energy than the completely dry state and where neither the coalesced nor the pinned meniscus morphology are stable. Owing to the re-entrant mechanical stability of the pinned meniscus morphology in base orientation at fixed aspect ratio AR , this wicking region in the plane spanned by the pair (LF, AR) assumes the form of a tongue entering the stability diagram from above. LF . The existence of the re-entrant regions of the line fraction for stable pinned menisci in base orientations cannot be explained by thermodynamic arguments or simple geometrical models and is a consequence of the suppression of coalescence instabilities of the pinned meniscus morphology at small line fractions. Coalescence of menisci in base orientation at a material contact angle of $\theta_0 = 52^\circ$ is not observed in our numerical results, even for triangular posts with high aspect ratio up to $AR \approx 4$. It has been

previously shown that the coalescence instability is suppressed for tall square posts if the contact angle exceeds a certain threshold value¹³. A contact angle sensitive mechanism similar to the coalescence instability has been proposed to explain the directional spontaneous imbibition observed in micro-grooves with asymmetric saw-tooth shaped walls²³.

Furthermore, the terminal meniscus in the triangular post array will always spontaneously coalesce for a contact angles $\theta_0 < 45^\circ$, irrespective of the orientation. Since the lines of the touch instability for menisci in tip, side and base orientation are very close for the particular geometry considered in the present work, directional wicking will hardly be observed for low contact angles. The preferential wicking in base direction reported by Jokinen et al.¹² for a material contact angles θ_0 in the range between 20° and 40° is presumably controlled exclusively by the touch instability of the coalesced meniscus. In contrast to the present work, the study of Jokinen et al.¹² considers a regular array of pointed triangular posts with small aspect ratio and large line fractions. For this geometry, spontaneous wicking in base direction observed for contact angles $\theta_0 < 45^\circ$ can be readily explained from the distance between the contact line of the coalesced terminal meniscus and the base of the post in the following dry row being smaller in tip orientation as compared to base orientation¹².

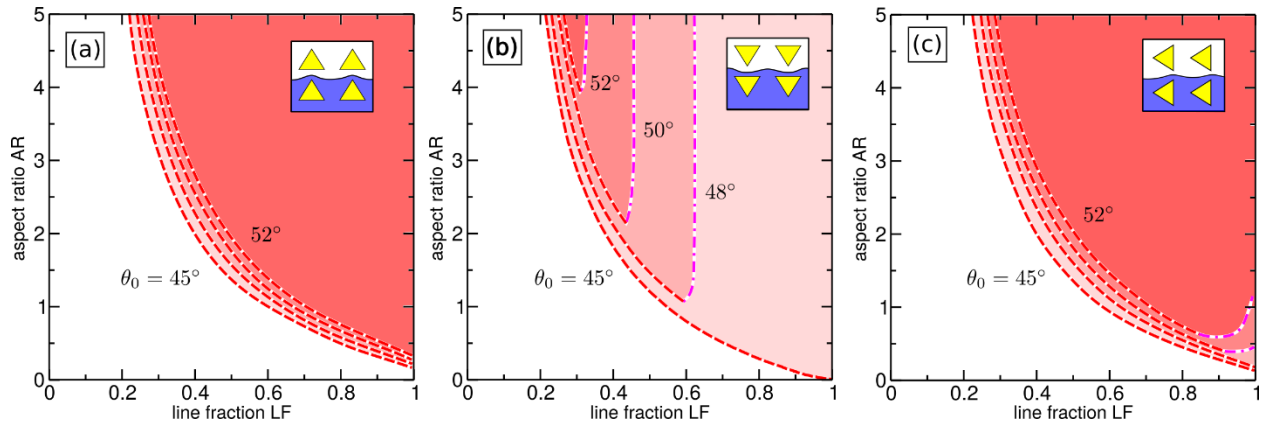


Figure 9. Stability diagram showing regions of line fraction LF and aspect ratio AR where spontaneous wicking is expected for a terminal meniscus in tip orientation (a), base orientation (b), and in side orientation (c). Each panel shows the boundary lines limiting the region where neither the coalesced nor the pinned meniscus morphology are found in our numerical energy minimizations for a Young's contact angle θ_0 of 45° , 48° , 50° , and 52° .

Figure 10 shows an overlap of the predicted regions of spontaneous wicking for menisci in tip, base and side orientation for a Young's contact angle of $\theta_0 = 50^\circ$ that are displayed in Fig. 9 (a-c) along with the experimentally observed wicking directions in our experiments, as indicated by symbols with corresponding colors. Apparently, the boundary lines of the spontaneous wicking region in tip, base, and side orientation allow only three scenarios: (i) non-wicking, (ii) directional wicking, and (iii) all-directional wicking. The observation of only these three wicking scenarios as well as the positions of the experimental data points display a strong correlation with the regions of the respective wicking regimes found in our numerical energy minimizations.

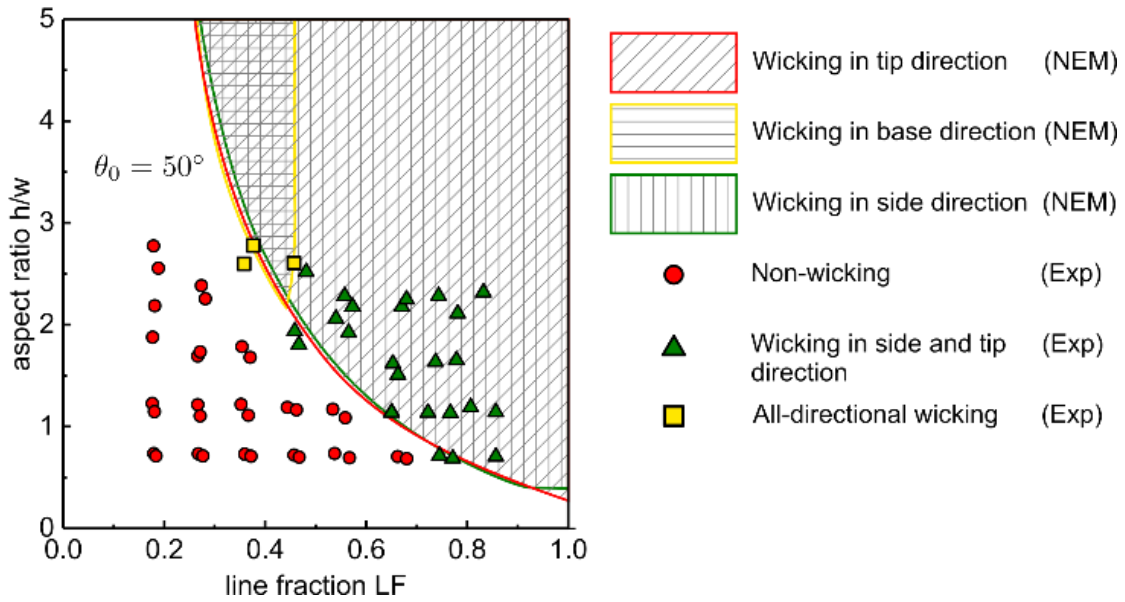


Figure 10. Comparison of the results from experiments (Exp) and Numerical energy minimizations (NEM). The differently hatched regions represent the wicking regimes in tip, base, and side orientation according to the results of our NEM for a Young's contact angle $\theta_0 = 50^\circ$. Symbols indicate the experimentally observed wicking scenarios; the size of the experimental error in aspect ratio AR and line fraction LF in average is similar to the symbol size.

The numerical results show that the region of wicking in base orientation is highly sensitive to the advancing contact angle and lowering the contact angle by only 2° may lead to a noticeable enlargement of regions where all-directional wicking is observed. Therefore, it is crucial for practical applications that rely on the transition between all-directional wicking and no-wicking or directional wicking behavior to carefully characterize the substrate material in terms of the advancing contact angle.

Although the predictions of numerical energy minimizations seem to capture the wetting phenomena on the triangular post structured surfaces well, the suitable contact angle to compare the numerical calculations to the experiments is slightly different. In this study, a Teflon coated surface is utilized, on which the heptane has a static advancing contact angle $\theta_a = (51.6 \pm 1.0)^\circ$ and a static receding contact angle $\theta_r = (42.7 \pm 1.2)^\circ$, as determined on a smooth reference surface. As we restrict on wicking in this paper, it is certainly save to assume the advancing contact angle, θ_a , is governing the wicking behavior. This is in contrast to the case of de-wicking, where the receding contact angle, θ_r , would be the relevant wetting parameter. The reason why the experimentally observed wicking behavior for a contact angle $\theta_a = (51.6 \pm 1.0)^\circ$ agree well with the numerical results that were determined for $\theta_0 = 50^\circ$ can most likely be attributed to slight imperfections of the Teflon coating on the micro-patterned substrates.

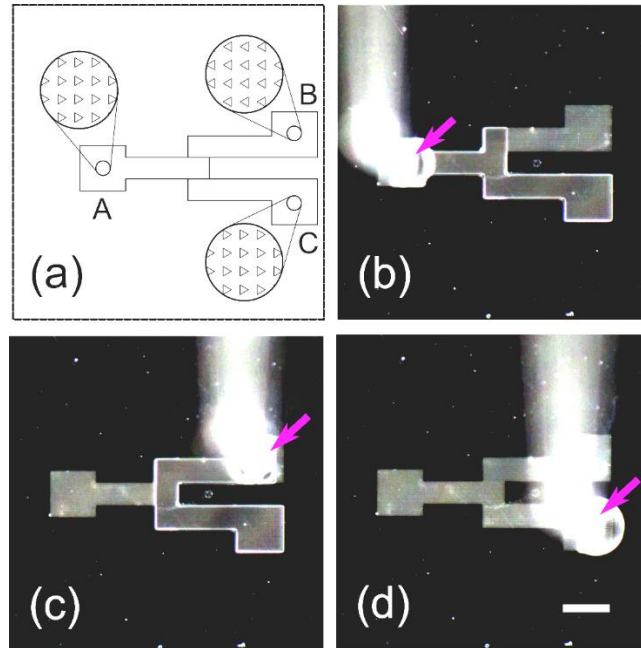


Figure 11. A liquid rectifier consisting of three connected channels structured with various post orientations. (a): Schematic illustration of the channel design. Alignment of the triangular posts is as indicated. The triangular posts have a dimension of $w = 16.4 \mu\text{m}$, $LF = 0.59$, and $AR = 1.65$. As in the previous experiments is $\theta_a = (51.6 \pm 1.0)^\circ$. (b): Injection at position A, wicking to C and not to B. (c): Injection at position B, wicking to C, and not to A. (d) Injection at position C and no wicking to A or B. The structured area turns into darker grey while wetted and the boundary of the wetted area appears bright. Pink arrows indicate the tips of injecting needle while the scale bar represents 1.0 mm.

Applications of directional wicking: To demonstrate that directional wicking is of practical use we created a “liquid rectifier” with three branches as shown in Fig. 11. The micro-fluidic rectifier consists of three micro-patterned stripes that are connected to a central junction, cf. the sketch in Fig. 11 (a). The line fraction $LF = 0.59$ and the aspect ratio $AF = 1.65$ of the triangular post arrays are chosen to be in the region of control parameters corresponding to directional wicking. For this post geometry wicking occurs only for terminal menisci of the film in tip and side orientation while wicking of a meniscus in base orientation is suppressed.

In this rectifier design, the triangular posts in the left and the lower right stripe are identically oriented. Posts in the upper right stripe, however, point into the opposing direction. The image shown in Fig. 11 (b) illustrates the principal functioning of the rectifier: liquid deposited on patch A will be wicked to patch C but at the same time does not reach to patch B. However, if liquid is deposited on patch B, the wicking film arrives at patch C while, at the same time, wicking of the liquid to patch A is suppressed, cf. Fig. 11(c). And finally, if the liquid is deposited on patch C, wicking toward both patch A and B is not allowed, and the liquid forms a sessile droplet instead. In summary, the rectifier can be used to supply liquids to the patch C from either patch A or B without the risk of contamination. More complex designs can be realized, as an anisotropic microfluidic cross, cf. Fig. S1 in the Supporting Information.

Besides of the directional wicking in tip and side directions, more types of directional wicking are found if we abandon the convention to consider equal line fractions in either directions of the post array. Different wicking scenarios can also be attained solely by changing either the lateral line fraction LLF or the vertical line fraction VLF . Figure 12 compares structures showing wicking only in the tip direction and wicking in both tip and base directions with non-equal LLF and VLF . These properties manifest a great flexibility and potential for functional surface applications.

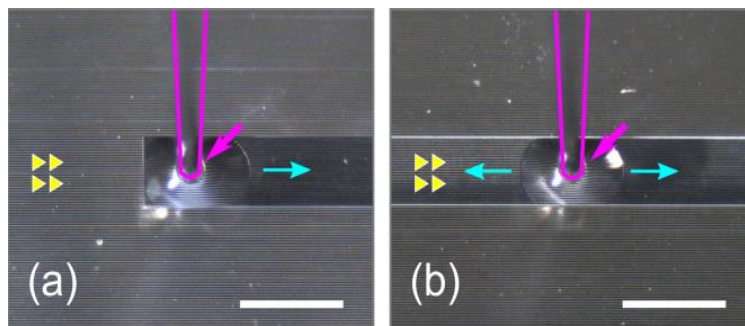


Figure 12: Different types of directional wicking obtained on surfaces patterned with triangular post having different lateral line fraction LLF and vertical line fraction VLF and aspect ratio AR . Advancing contact angle of the test liquid is $\theta_a = (51.6 \pm 1.0)^\circ$. (a): Wicking only in the tip direction ($LLF = 0.34$, $VLF = 0.84$, $AR = 1.19$). (b): Wicking in the tip and base directions ($LLF = 0.37$, $VLF = 0.67$, $AR = 1.70$). Pink outlines and arrows indicate the position of the needles and needle tips. Blue arrows represent the wicking directions. Yellow triangles indicate post alignment. The scale bars represent 2.0 mm.

Conclusions and Outlook

In this work we investigated the onset of wicking of a liquid film into a regular micro-pattern of posts with homogeneous triangular cross-section. For the sake of clarity, and to ease comparison to numerical results, we focused our work on post arrays with equal lateral and vertical line fraction where two mechanically stable morphologies of the terminal meniscus could be identified in our numerical energy minimizations. These interfacial morphologies termed *coalesced* meniscus and *pinned* meniscus differ in the topology of the three phase contact line on the bottom surface. Their appearances are limited to certain regions of the line fraction and aspect ratio of the posts. Results of our numerical energy minimizations show that the extension and shape of these regions depend on the relative orientations of the meniscus with respect to the underlying pattern of triangular posts.

Our results also corroborate the criterion that spontaneous wicking is observed on post arrays where none of the two possible meniscus configurations are mechanically stable and where the interfacial free energy of the complete film state is lower than the one of the dry state. This led us to conclude that the essential physics of wicking is captured already by the mechanical stability and the interfacial free energy of certain morphologies of the leading edge of the liquid film. The material contact angle has a strong influence on the range of pattern geometries where both meniscus morphologies can exist as stable shapes in certain orientations and, thus, on the emergence of directional wicking.

In an array of triangular posts, the motion of a wicking liquid film is governed both by the touch instability of the coalesced meniscus morphology and by the coalescence instability of the pinned meniscus morphology. As the touch instability is rather insensitive to the orientation of the posts relative to the meniscus, directional wicking in the triangular post arrays is largely controlled by

the coalescence instability of the pinned meniscus morphology. Choosing a test liquid with an advancing contact angle of 50° allowed us to observe the transition from all directional wicking in arrays of high aspect ratio posts to directional wicking in tip and side direction in arrays with lower aspect ratios. Our numerical investigations for a series of contact angle between 45° and 52° and previous investigations for arrays of posts with square and circular cross-sections suggest that coalescence will be effectively suppressed in arrays of triangular posts with arbitrary aspect ratios for liquids with advancing contact angles up to a material contact angles around 60° .

As evidenced in demonstration experiments, the directional selectivity of spontaneous wicking in arrays of triangular posts has potential applications in devices relying on passive liquid transport. Directional wicking in channels with different post orientations or with posts of different geometries enables a precise control of liquid transport as required in logical units such as the liquid rectifiers considered here. The latter can be exploited to build interfaces to feed liquid samples into microfluidic devices or for open micro-fluidics, e.g., to guide liquids from different positions at desired locations in medical applications without the risk of contaminations. Provided the contact angles of the two liquids differ, such a device could be designed to function only if these liquids are applied at their designated inlet and, thus, to prevent faulty operation.

So far, we did not test our micro-patterned samples for spontaneous de-wicking. Here, we expect a larger number of possible interface morphologies after retraction of the film that need to be considered in numerical energy minimizations. A systematic study of the intrinsic time-scales of the coalescence and touch instabilities could help to develop a dynamic model to predict the velocities of the wicking film for different orientations of the leading film edge. Further studies of directional de-wicking and an assessment of the thermodynamic condition in comparison the numerically determined criteria of mechanical stability will be subject of a forthcoming article.

Supporting Information: Images of the microfluidic cross and characterizations of all micro-pattern geometry of samples used in experiments are given in the supporting information (PDF).

Author Contribution

The manuscript was written through contributions of all authors. All authors have given approval to the final version of the manuscript.

Acknowledgement. We thank V. Jokinen for useful comments and for pointing our attention to Ref.¹². The research was supported by a bilateral program of the Taiwanese Ministry of Science and Technology (MOST) and the Deutsche Forschungsgemeinschaft (DFG) under the grant no. MOST106-2923-E002-016 and SE 1118/8, respectively.

References

- (1) Blossey, R. Self-Cleaning Surfaces - Virtual Realities. *Nat. Mater.* **2003**, 2 (5), 301–306.
- (2) Zheng, Y.; Gao, X.; Liang, L. Directional adhesion of superhydrophobic butterfly wings. *Soft Matter* **2007**, 3, 178-182.
- (3) Ju, J.; Bai, H.; Zheng, Y.; Zhao, T.; Fang, R.; Jiang, L. A Multi-Structural and Multi-Functional Integrated Fog Collection System in Cactus. *Nat. Commun.* **2012**, 3 (1), 1247.
- (4) Comanns, P.; Buchberger, G.; Buchsbaum, A.; Baumgartner, R.; Kogler, A.; Bauer, S.; Baumgartner, W. Directional, Passive Liquid Transport: The Texas Horned Lizard as a Model for a Biomimetic “Liquid Diode”. *J. R. Soc. Interface* **2015**, 20150415.
- (5) Chu, K. H.; Xiao, R.; Wang, E. N. Uni-Directional Liquid Spreading on Asymmetric Nanostructured Surfaces. *Nat. Mater.* **2010**, 9 (5), 413-417.
- (6) Jokinen, V. Directional Imbibition on a Chemically Patterned Silicon Micropillar Array. *Soft Matter* **2016**, 12 (4), 1100-1106.
- (7) Seemann, R.; Brinkmann, M.; Kramer, E. J.; Lange, F. F.; Lipowsky, R. Wetting Morphologies at Microstructured Surfaces. *Proc. Natl. Acad. Sci.* **2005**, 102 (6), 1848-1852.
- (8) Herminghaus, S.; Brinkmann, M.; Seemann, R. Wetting and Dewetting of Complex Surface Geometries. *Annu. Rev. Mater. Res.* **2008**, 38 (1), 101-121.
- (9) Xia, D.; He, X.; Jiang, Y.-B.; Lopez, G.P; Brueck, S.R.J. Tailoring Anisotropic Wetting Properties on Submicrometer-Scale Periodic Grooved Surfaces. *Langmuir* **2010**, 26 (4), 2700-2706.
- (10) Semprebon, C.; Herrmann, C.; Liu, B.-Y.; Seemann, R.; Brinkmann, M. Shape Evolution

- of Droplets Growing on Linear Microgrooves. *Langmuir* **2018**, *34* (36), 10498-10511.
- (11) Courbin, L.; Denieul, E.; Dressaire, E.; Roper, M.; Ajdari, A.; Stone, H. A. Imbibition by Polygonal Spreading on Microdecorated Surfaces. *Nat. Mater.* **2007**, *6* (9), 661-664.
 - (12) Jokinen, V.; Leinikka, M.; Franssila, S. Microstructured surfaces for directional wetting. *Adv. Mater.* **2009**, *21*, 4835-4838.
 - (13) Blow, M.; Kusumaatmaja, H.; Yeomans, J. Imbibition through an array of triangular posts. *J. Phys. Condensed. Mat.* **2009**, *21*, 464125.
 - (14) Semprebon, C.; Forsberg, P.; Priest, C.; Brinkmann, M. Pinning and Wicking in Regular Pillar Arrays. *Soft Matter* **2014**, *10* (31), 5739-5748.
 - (15) Law, K.-Y.; Zhao, H. Contact Angle Measurements and Surface Characterization Techniques. In *Surface Wetting*; 2015; pp 7-34.
 - (16) Yeh, K. Y.; Cho, K. H.; Yeh, Y. H.; Promraksa, A.; Huang, C. H.; Hsu, C. C.; Chen, L. J. Observation of the Rose Petal Effect over Single- and Dual-Scale Roughness Surfaces. *Nanotechnology* **2014**, *25*, 345303.
 - (17) Eral, H. B.; De Ruiter, J.; De Ruiter, R.; Oh, J. M.; Semprebon, C.; Brinkmann, M.; Mugele, F. Drops on Functional Fibers: From Barrels to Clamshells and Back. *Soft Matter* **2011**, *7*, 5138-5143.
 - (18) Hofmann, T.; Tasinkevych, M.; Checco, A.; Dobisz, E.; Dietrich, S.; Ocko, B. M. Wetting of Nanopatterned Grooved Surfaces. *Phys. Rev. Lett.* **2010**, *104* (10), 106102.
 - (19) Brakke, K. A. The Surface Evolver. *Exp. Math.* **1992**, *1* (2), 141-165.
 - (20) Yao, M.; Fang, J. Hydrophilic PEO-PDMS for Microfluidic Applications. *J. Micromechanics Microengineering* **2012**, *22* (2), 025012.
 - (21) Yao, X.; Hu, Y.; Grinthal, A.; Wong, T.-S.; Mahadevan, L.; Aizenberg, J. Adaptive Fluid-Infused Porous Films with Tunable Transparency and Wettability. *Nat. Mater.* **2013**, *12* (6), 529-534.

- (22) Concus, P.; Finn, R.; On the behavior of a capillary surface in a wedge. *PNAS* **1969**, *63* (2), 292-299.
- (23) Feng, J.; Rothstein, J. P. One-way wicking in open micro-channels controlled by channel topography. *J. Coll. Interface Sci.* **2013**, *404*, 169-178.

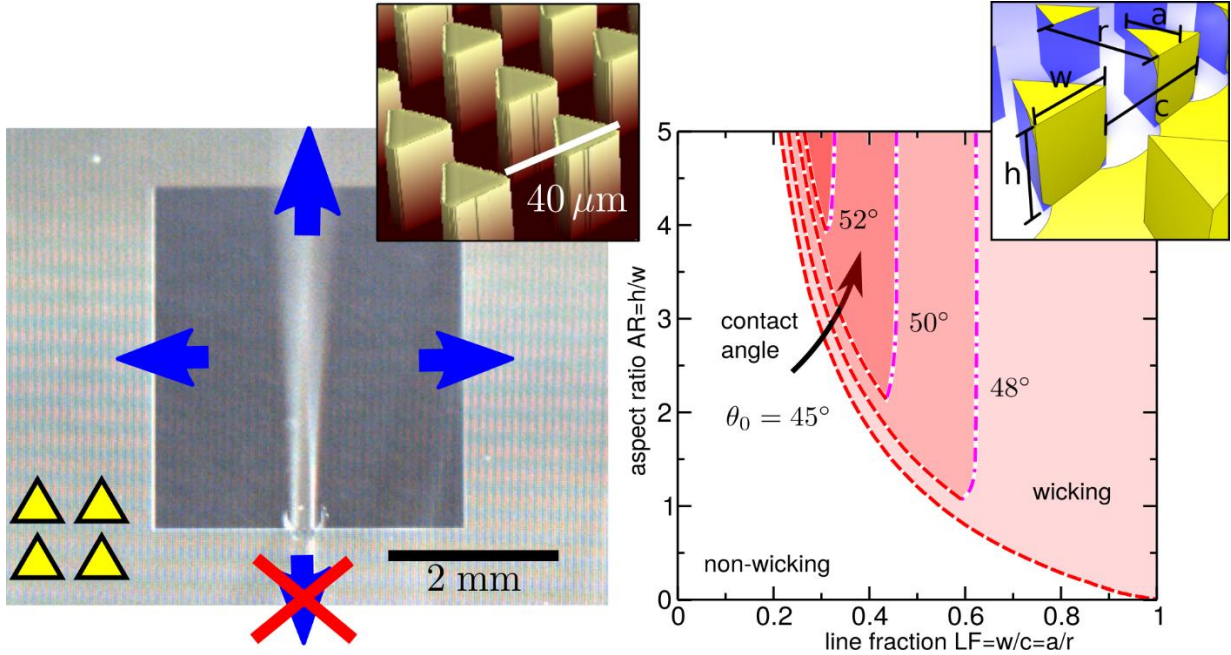


Table of content graphics